catalysts

MDPI

Article

Al_2O_3-Supported Transition Metals for Plasma-Catalytic NH_3 Synthesis in a DBD Plasma: Metal Activity and Insights into Mechanisms

Yury Gorbanev [1,*], Yannick Engelmann [1], Kevin van't Veer [1,2], Evgenii Vlasov [3], Callie Ndayirinde [1], Yanhui Yi [4], Sara Bals [3] and Annemie Bogaerts [1]

1 Research Group PLASMANT, Department of Chemistry, University of Antwerp, Universiteitsplein 1, 2610 Antwerp, Belgium; yannick.engelmann@uantwerpen.be (Y.E.); kevin.vantveer@uantwerpen.be (K.v.V.); callie.ndayirinde@uantwerpen.be (C.N.); annemie.bogaerts@uantwerpen.be (A.B.)
2 Chemistry of Surfaces, Interfaces and Nanomaterials (ChemSIN), Faculty of Sciences, Université Libre de Bruxelles, Avenue F. D. Roosevelt 50, 1050 Brussels, Belgium
3 Research Group EMAT, Department of Physics, University of Antwerp, Groenenborgerlaan 171, 2020 Antwerp, Belgium; evgenii.vlasov@uantwerpen.be (E.V.); sara.bals@uantwerpen.be (S.B.)
4 State Key Laboratory of Fine Chemicals, School of Chemical Engineering, Dalian University of Technology, Dalian 116024, China; yiyanhui@dlut.edu.cn
* Correspondence: yury.gorbanev@uantwerpen.be; Tel.:+32-32652343

Abstract: N_2 fixation into NH_3 is one of the main processes in the chemical industry. Plasma catalysis is among the environmentally friendly alternatives to the industrial energy-intensive Haber-Bosch process. However, many questions remain open, such as the applicability of the conventional catalytic knowledge to plasma. In this work, we studied the performance of Al_2O_3-supported Fe, Ru, Co and Cu catalysts in plasma-catalytic NH_3 synthesis in a DBD reactor. We investigated the effects of different active metals, and different ratios of the feed gas components, on the concentration and production rate of NH_3, and the energy consumption of the plasma system. The results show that the trend of the metal activity (common for thermal catalysis) does not appear in the case of plasma catalysis: here, all metals exhibited similar performance. These findings are in good agreement with our recently published microkinetic model. This highlights the virtual independence of NH_3 production on the metal catalyst material, thus validating the model and indicating the potential contribution of radical adsorption and Eley-Rideal reactions to the plasma-catalytic mechanism of NH_3 synthesis.

Keywords: nitrogen fixation; ammonia; non-thermal plasma; plasma catalysis; dielectric barrier discharge; Eley-Rideal mechanism; model validation

Citation: Gorbanev, Y.; Engelmann, Y.; van't Veer, K.; Vlasov, E.; Ndayirinde, C.; Yi, Y.; Bals, S.; Bogaerts, A. Al_2O_3-Supported Transition Metals for Plasma-Catalytic NH_3 Synthesis in a DBD Plasma: Metal Activity and Insights into Mechanisms. *Catalysts* **2021**, *11*, 1230. https://doi.org/10.3390/catal11101230

Academic Editor: Vasile I. Parvulescu

Received: 24 September 2021
Accepted: 9 October 2021
Published: 13 October 2021

1. Introduction

The continuous growth of the world's population sets a demand for the increased production of food. Nitrogen is one of the key elements in fertilisers required for the plant growth to meet this demand. The paramount step in this process is making the chemically inert atmospheric N_2 into accessible nitrogen. Nitrogen fixation is, therefore, one of the most important tasks of chemical industry.

Since the beginning of the 20th century, when the Haber-Bosch (HB) process was introduced [1], fertilisers based on ammonia (NH_3) have been produced synthetically in quantities which exceed the naturally occurring N_2 fixation by orders of magnitude [2]. Today, approximately half of the world's population depends on the production of NH_3 via the HB process [3]. Besides the agricultural sector, NH_3 is also used as a base chemical in the production of pharmaceuticals and plastics, in the textile, metallurgical, and automotive industry [1,4,5], as well as a carbon-free fuel [6].

The HB process, while dominating the chemical industry, is currently still unsustainable. It operates at high temperatures and pressures, consumes 1.8% of the global energy supply, and produces large amounts of CO_2 which constitute 1.5% of the global CO_2 emissions [7,8]. Naturally, more sustainable and benign alternatives to the thermocatalytic HB process are under avid investigation. HB electrification, for example, could potentially offer reduced CO_2 emissions and lower overall energy consumption, but does not substantially decrease the need for centralised production, required for HB to be energy efficient [8].

Other approaches which avoid HB altogether have been gaining increased attention over the past decades [9]. Novel bio-technological solutions, together with thermal, photo-, and electro-catalytic processes, have been proposed as greener substitutes for HB [10–12]. Among other techniques, plasma-based N_2 fixation is of high interest due to the flexibility of its use and synergy with sustainable energy sources, i.e., renewable electricity [13,14].

In short, plasma is a partially ionised gas and can be obtained by applying an electric field to gas causing a breakdown, which produces a wide range of reactive species: electrons, ions, radicals, excited species, and photons [13,15]. Various plasma-based processes have been under investigation for NH_3 production in recent years. N_2 fixation was achieved by plasma, plasma-catalytic, and plasma-electrocatalytic processes. Moreover, different pathways leading from N_2 to NH_3 were investigated. Among these are reduction of the plasma-produced NO_x to NH_3 [16,17], and direct reactions of N_2 with H_2 [18,19] or H_2O [20–22], as also summarised in detail in recent reviews [23,24]. We show the possible pathways of the plasma-driven N_2 fixation in Figure 1. Here, plasma-catalytic synthesis of NH_3 from N_2 and H_2 is the most direct alternative to the energy-intensive HB process. Plasma catalysis (PC) for NH_3 production is of particular interest because of the synergy between the two techniques [25,26]: plasma-enabled excitation and dissociation of N_2 molecules allows NH_3 yields beyond values attainable by thermal catalysis [27].

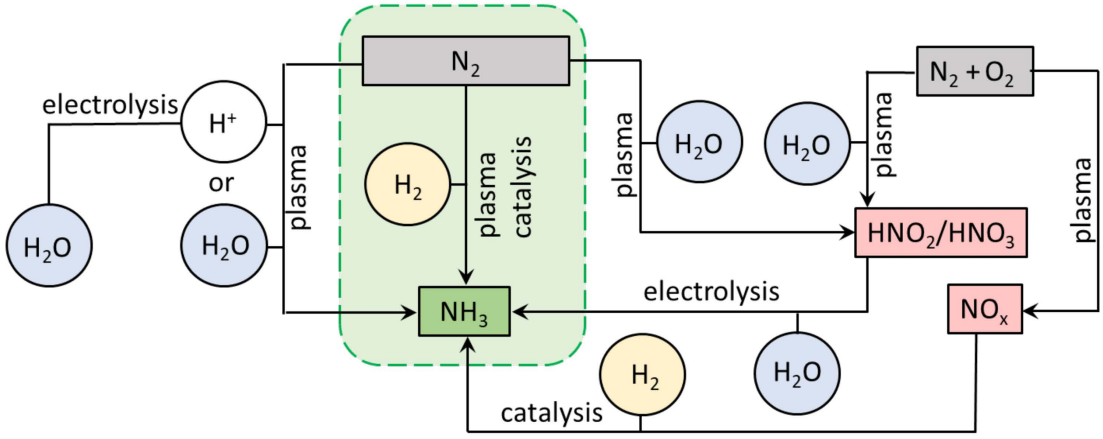

Figure 1. Various pathways of plasma-driven NH_3 production from N_2. The green frame focuses on plasma catalysis described in this work.

Dielectric barrier discharge (DBD) plasma reactors are the most common choice for PC NH_3 synthesis [28]. DBD plasma is a type of non-thermal plasma, in which the electrons are at high temperature (10^4–10^5 K), while the gas remains at 300–1000 K [13]. DBD produces highly energetic, spatially and temporally non-uniform microdischarges (filaments) [28]. Therefore, the high energy density of the filaments allows excitation of molecules by plasma but limits the overall gas heating, thus reducing the potential thermal NH_3 decomposition [18].

Some of the first reports of PC NH_3 production from N_2 and H_2 in DBD describe reactors with Al_2O_3-coated inner walls of the reactor [29], as well as Ru deposited on the Al_2O_3 inner walls [30]. A decade later, the interest to PC synthesis of NH_3 was re-kindled, when Gomez-Ramirez et al. reported NH_3 production using lead zirconium titanate (PZT) and $BaTiO_3$ as catalysts in a packed bed [31]. Since then, many catalysts comprised of

various active metals on different supports have been employed, including Au, Pt, Ag, Cu [32,33], Ru-Cs supported on carbon nanotubes [34], RuO_2-CsO/MgO [35], Ni/SiO_2 [36], etc. Moreover, numerous catalysts supported on Al_2O_3 beads or pellets were used, e.g., Ni, Co, Ru, Pt, Rh [19,27,37–39]. A summary of the state-of-the-art on plasma-catalytic NH_3 synthesis, based on literature reports since 2004 up to 2021, in terms on energy consumption, N_2 conversion, NH_3 yield, and production rate, along with the corresponding catalysts used and the relevant operating conditions, is shown in a table in the Discussion section below. In general, Al_2O_3 and other beads are often used as supports for catalysts used in PC. These macrostructures are packed in a catalyst bed with gaps between the beads, thus allowing for the gas in the flow plasma reactor (such as DBD) to pass through without creating overpressure, as, e.g., a powder-packed bed would [28,40].

In the last three years, the growing interest in PC NH_3 has led to numerous studies which attempted to discriminate between the plasma and thermal catalytic effects in PC, identify the mechanisms of PC NH_3 formation, and formulate the differences between thermal and plasma catalysis [13,18,37]. However, despite the substantial progress in the field of PC, many unknowns still linger. For example, for the NH_3 synthesis, by thermal catalysis, the "volcano" plot refers to the relative activity of different metals, with some metals being most active for the NH_3 production, thus occupying the peak of the "volcano" [41]. Recent advances in microkinetic computational modelling suggest that, in plasma catalysis, the relative NH_3 synthesis rates on different metal catalysts (i.e., the catalytic "volcano" plot as described above) are different from those in thermal catalysis for the same catalysts, due to the interaction of vibrationally excited N_2 with the catalyst material [42]. Our previous computational study expanded on this topic, with the results indicating that the presence of radicals in the plasma could activate catalyst materials via radical adsorptions and Eley-Rideal (ER) reactions, on top of Langmuir-Hinshelwood (LH) reactions in thermal catalysis [43]. In practice, radical reactions provided a possible explanation for the high reactivity of both noble and non-noble metals, which was not predicted by thermal trends nor trends induced by vibrationally excited N_2 molecules [43].

In the present work, we studied the performance of four different metal catalysts (Ru, Fe, Co, and Cu) supported on γ-Al_2O_3 beads for the production of NH_3 from N_2 and H_2 in a DBD plasma reactor. These catalysts represent a range of catalyst binding strengths: optimal for thermal HB (Ru), more strongly binding and mostly used in industrial HB (Fe) [5], more weakly binding and predicted to be optimal for the levels of vibrational excitation occurring in DBDs (Co) [42,43], and a noble catalyst predicted to be active only in the presence of radical reactions (Cu) [43]. We evaluated the amount of produced NH_3 and the energy consumption (EC) of the process. We also analysed the catalyst surface using scanning electron microscopy and energy dispersive X-ray spectroscopy in a scanning electron microscope (SEM-EDX), high-angle annular dark-field scanning transmission electron microscopy (HAADF-STEM), and N_2 physisorption. We evaluated the turnover frequency (TOF) values of the catalysts. Based on the obtained results, we evaluated the possibility of different types of reaction mechanisms in the PC NH_3 synthesis.

2. Results

2.1. Catalyst Characterisation

Four 10 wt% Al_2O_3-supported catalysts were prepared by incipient wetness impregnation of γ-Al_2O_3 beads. Water soluble salts of the respective metals (Fe, Ru, Co, Cu) were used as precursors. The detailed procedure of catalyst preparation is described in the Materials and Methods section below. The X-ray powder diffractograms (XRPD) of some of the catalysts are shown in Figure S1 in the Supplementary Materials.

In preliminary experiments, we prepared 1 wt% catalysts. They did not show any activity in our plasma-catalytic NH_3 synthesis beyond that of the pristine Al_2O_3 beads. Because the purpose of this work was to study the relative effects of catalyst activity rather than optimising the reaction parameters, we used the beads with 10 wt% of the respective

metals in order to enable the comparison of metal activity. The 10 wt% metal loading clearly had a strong catalytic effect as demonstrated below (see Section 2.2).

The catalysts were also characterised by N_2 physisorption, as shown in Table 1 below. The experimental details of this and other analytical techniques used in this work can be found in Materials and Methods. The catalysts were reduced prior to BET and electron microscopy analyses [44].

Table 1. Active surface area and pore volume of the different 10 wt% Al_2O_3-supported metal catalysts, as well as the pristine Al_2O_3.

Material	S_{BET} (m^2/g)	V (cm^3/g)
Al_2O_3	321	n/a
10 wt% Fe/Al_2O_3	204	0.42
10 wt% Ru/Al_2O_3	144	0.29
10 wt% Co/Al_2O_3	175	0.37
10 wt% Cu/Al_2O_3	203	0.42

The active surface area S_{BET} of the material decreased compared to the pristine Al_2O_3, as anticipated: part of the surface pores was covered with metal particles. The extent of this decrease was similar for all catalysts, although Ru/Al_2O_3 exhibited the lowest (144 m^2/g) surface area. Likewise, the pore volume V was found to be similar for all catalysts, with Ru/Al_2O_3 once again having the lowest pore volume (0.29 cm^3/g). Nonetheless, the obtained data reveal that both the surface area and pore volume of all materials are in the same order of magnitude. Importantly, the surface area and pore volume of the catalysts did not change upon plasma exposure, as shown on the example of the Co catalyst (Supplementary Materials, Table S1). Due to the non-thermal nature of the DBD plasma, the temperature of the gas during the plasma-catalytic NH_3 synthesis is much lower than in thermal catalysis. However, the localised microscale temperature on the surface of the beads can reach high values due to the direct interaction with the high energy filaments [45]. This could lead to changes of the catalyst surface properties during plasma exposure [46]. Nonetheless, our results suggest that such changes did not occur, or at least not to a large extent, likely because the temperature was below the detrimental values.

Further, the amount of the deposited metal was evaluated using SEM-EDX, which allows accurate estimation of the metal content during elemental analysis, comparably, e.g., to the ICP-AES technique [47]. The 2D SEM images with respective EDX maps are shown in Figure S1 in Supplementary Materials.

The results presented in Table 2 demonstrate that the determined metal loading for the four catalysts was generally in good agreement with the 10 wt% loading calculated during the preparation. The discrepancies from the expected loading of 10 wt% arise from the facts that (i) the catalyst beads were powderised for the analysis with possible homogenisation limitations, and (ii) the inherently localised type of analysis (SEM-EDX). Considering these two factors, the analytical results are in good agreement with the value of 10 wt%, calculated during the catalyst preparation.

Table 2. Metal loading and average size of the particles for the different Al_2O_3-supported catalysts.

Catalyst	Metal Loading [1] (wt%)	Particle Size [2] (nm)
Fe/Al_2O_3	9.9 ± 0.7	5.7 ± 3.4
Ru/Al_2O_3	11.0 ± 1.1	7.5 ± 3.0
Co/Al_2O_3	8.6 ± 0.5	28.8 ± 17.8
Cu/Al_2O_3	12.1 ± 0.6	4.1 ± 2.7

[1] Determined by SEM-EDX analysis of the homogenised powder obtained by crushing the beads of the respective catalyst. The shown error margins represent the values of the standard deviation obtained from the analyses of different regions of the same sample. [2] Estimated by HAADF-STEM analysis of the powderised beads.

The average particle size (Figure 2, as well as Table 2) was calculated from the particle size distribution data obtained by the HAADF-STEM analysis of the metal catalysts. During quantification, an effective diameter $d_{eff} = 2\sqrt{\frac{A_p}{\pi}}$ was assumed, where A_p is the measured area of the particle. While the other catalysts consisted mostly of nanoparticles of several nm in size (<10 nm), the Co nanoparticles had a different size distribution, with larger particles (>20 nm). However, using electron tomography (see below), a technique which yields a 3D visualisation of the samples based on a series of 2D images acquired along different viewing directions [48], we estimated the surface-to-volume ratios for the large Co and the small Ru nanoparticles. The two values were found to be quite similar: 1.8 and 2.3 nm^{-1}, respectively. Therefore, despite having larger (agglomerated) particles, the 10 wt% Co/Al_2O_3 catalyst can be directly compared to the other catalysts used in this work. This is especially important for the comparison of the TOF values discussed below: similar surface-to-volume ratios do not impact the TOFs differently. The representative 2D and 3D tomography images are shown in Figure 3.

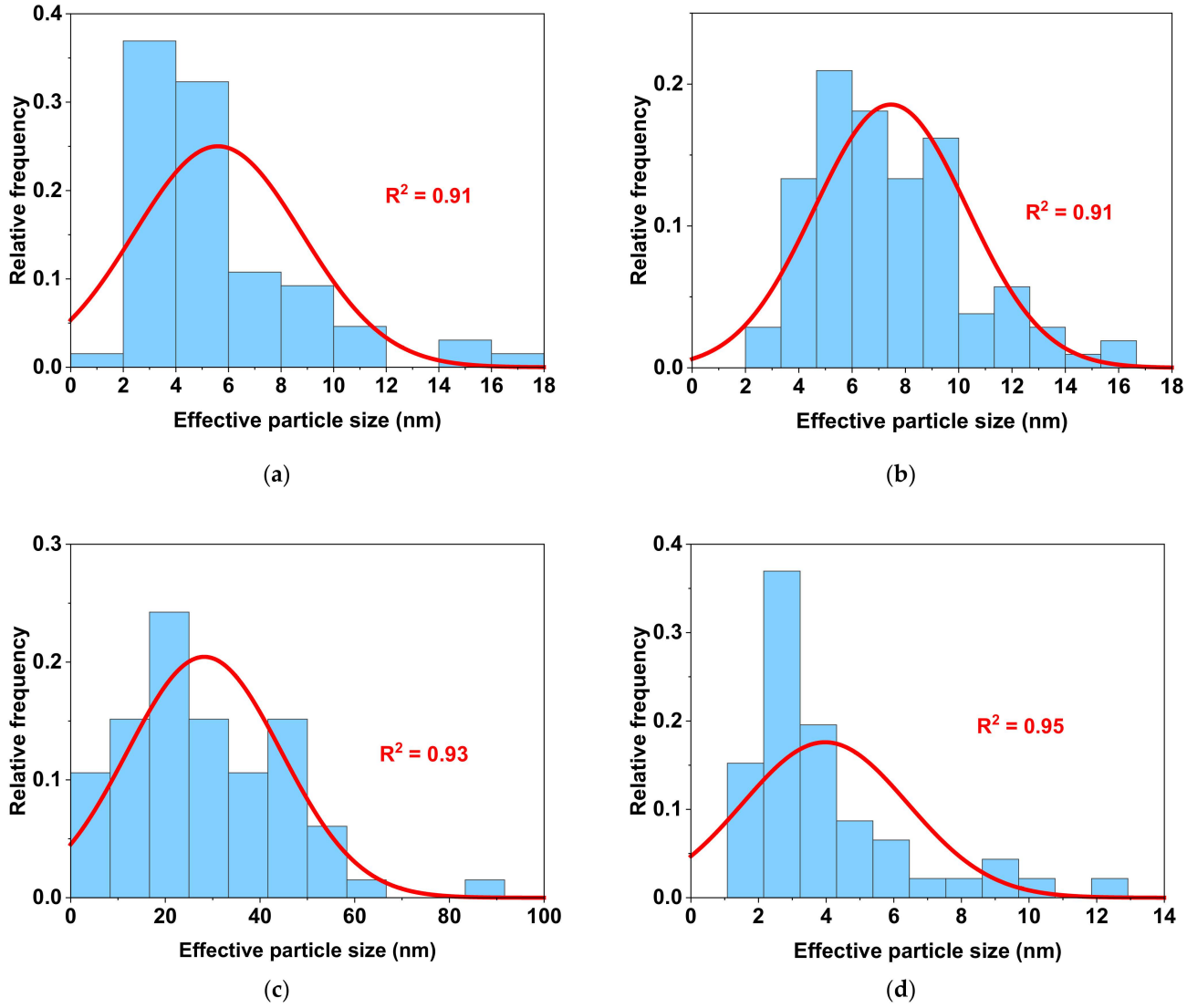

Figure 2. Size distribution of metal particles for the four Al_2O_3-supported catalysts, as determined by HAADF-STEM. (**a**) 10 wt% Fe/Al_2O_3, (**b**) 10 wt% Ru/Al_2O_3, (**c**) 10 wt% Co/Al_2O_3, and (**d**) 10 wt% Cu/Al_2O_3. The red curve is added for visualisation purposes and corresponds to the fitting of the experimental data with normal distribution. The numerical values of the mean particle size are presented in Table 2.

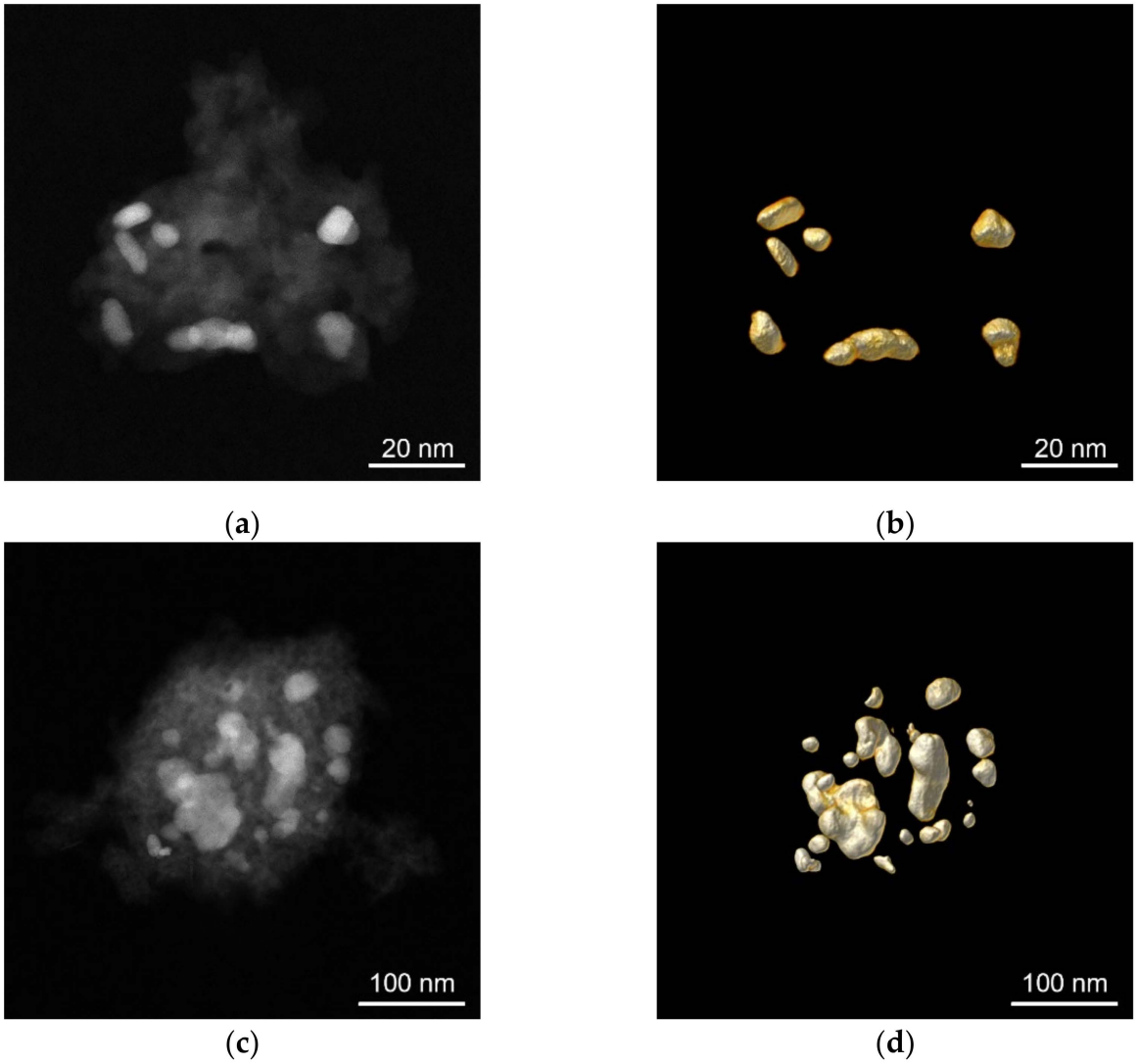

Figure 3. Typical 2D HAADF-STEM and reconstructed 3D images of the powderised beads of the Al_2O_3-supported metal catalysts. (**a**) 2D image of the 10 wt% Ru/Al_2O_3, (**b**) reconstructed 3D image of the Ru particles on Al_2O_3, (**c**) 2D image of the 10 wt% Co/Al_2O_3, and (**d**) reconstructed 3D image of the Co particles on Al_2O_3.

We also evaluated the metal coverage of the four catalysts (Table 3). The metal coverage was defined as the area covered by the metal sites, divided by the total area of the analysed material (metal sites and support). The metal coverage values were calculated by averaging the surface ratios based on several recorded 2D HAADF-STEM images. Importantly, we confirmed the applicability of such approach by calculating the coverage from 3D images by using electron tomography. Tilt series for electron tomography were acquired over an angular range of ±75° with a tilt increment of 3° using a Thermo Fischer Scientific aberration-corrected 'cubed' Titan (Waltham, MA, USA) operated at 300 kV. After alignment of the projection images by cross-correlation, stacks of aligned projection images served as an input for 15 iterations of the expectation maximisation reconstruction algorithm implemented in the ASTRA toolbox [49]. The obtained 3D data were first segmented manually. Next, the metal coverage was calculated as follows (Equation (1)):

$$\text{Metal coverage } (\%) = \frac{SA_P}{SA_P + SA_s} \times 100\% \,, \tag{1}$$

where SA_p is the surface area of the particles, and SA_s is the surface area of the support. Figure 4 shows representative 2D and 3D images obtained by electron tomography, for the example of the 10 wt% Fe/Al_2O_3 catalyst.

Table 3. Metal coverage, defined as ratio of the metal surface area to the total surface area, of the four different 10 wt% Al_2O_3-supported metal catalysts, obtained from 2D imaging and 3D processing by HAADF-STEM imaging.

Material	Average Metal Coverage (%)	
	Extracted from 2D Projection	Extracted from 3D Reconstruction
10 wt% Fe/Al_2O_3	14.9	10.4
10 wt% Ru/Al_2O_3	10.3	8.5
10 wt% Co/Al_2O_3	16.8	15.1
10 wt% Cu/Al_2O_3	6.7	n/a [1]

[1] The 3D tomography data could not be obtained due to the observed sensitivity of the sample to the electron beam irradiation at prolonged acquisition periods.

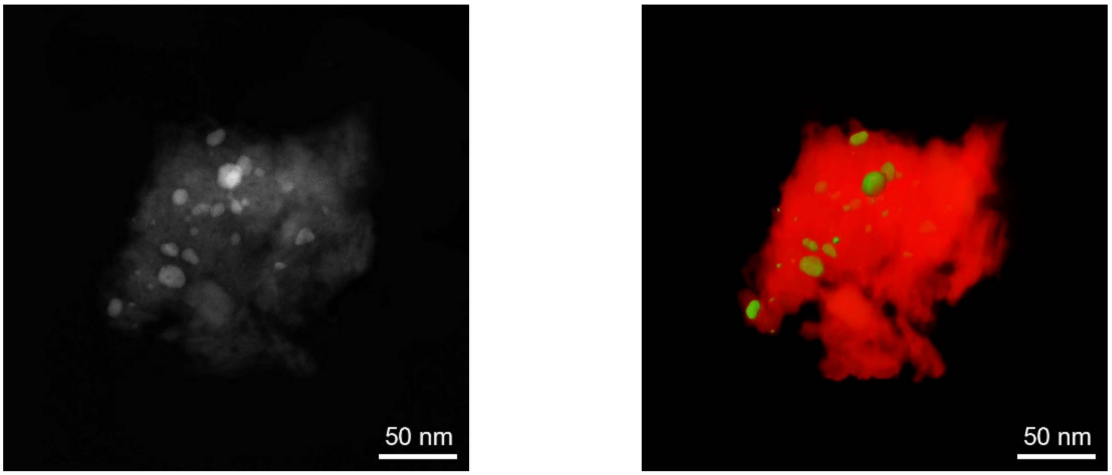

Figure 4. Results of electron tomography of the 10 wt% Fe/Al_2O_3 catalyst. (**a**) 2D image of the surface consisting of particles and support; (**b**) reconstructed 3D image of both the particles and the support. The support (Al_2O_3) is marked in red colour, and the Fe particles are marked in green.

The data shown in Table 3 indicate that the results extracted from 2D and 3D imaging by HAADF-STEM are comparable, confirming the applicability of this analytical approach albeit with precision limitations. We further used the obtained values of the metal coverage in the calculation of the TOFs for the different metals, as shown below in Section 2.2. We acknowledge that the used TOFs are only approximate here. Nevertheless, they are used to obtain semi-qualitative trends, rather than to compare exact values, as shown below.

2.2. Plasma-Catalytic NH_3 Formation: Performance of the Al_2O_3-Supported Catalysts

The PC NH_3 experiments were conducted in a cylindrical DBD reactor, operated with an AC current at 23.5 kHz frequency. The high voltage (HV) electrode covered a section of the dielectric barrier (ceramic tube), inside of which a ground electrode (stainless steel rod) was positioned.

The catalytic materials (Al_2O_3 beads impregnated with catalytically active metals) were introduced inside the gap between the dielectric barrier and the ground electrode, until the volume corresponding to the HV electrode length was filled with them. The plasma discharge occurred within the packed catalyst bed volume. The electrical characteristics of the plasma were monitored using voltage and current probes. The detailed description of the plasma setup is given in the Materials and Methods section below.

The schematic representation of the setup, including the reactor packed with catalyst beads, is shown in Materials and Methods. The electrical characteristics of the plasma, including the current and voltage profiles, and the Lissajous figures, are shown in Supplementary Materials, Figures S2 and S3. The plasma power was calculated from the Lissajous figures, i.e., from the charge-voltage characteristics, by integrating the area enclosed under the charge-voltage curves as described in literature [50,51]. The figures showed general similarity, not only for all catalysts but also for the three feed gas ratios (3:1, 1:1, 1:3 H_2:N_2), when using the same catalyst (Figure S3). The current and voltage profiles were similar for all Al_2O_3-supported catalysts and the pristine Al_2O_3, with the exception of Fe/Al_2O_3 for which the current waveform was different (Figure S2). This is in agreement with literature, where Fe catalysts were also found to be altering the characteristics of the discharge current [19]. However, the important finding was that the plasma power remained virtually identical for all experimental conditions investigated, i.e., for all supported catalysts independently of the metal, as well as for the empty reactor and the pristine support (Figure 5). This is also in good agreement with literature [52] and allows comparison of product yields and EC values between the various catalysts.

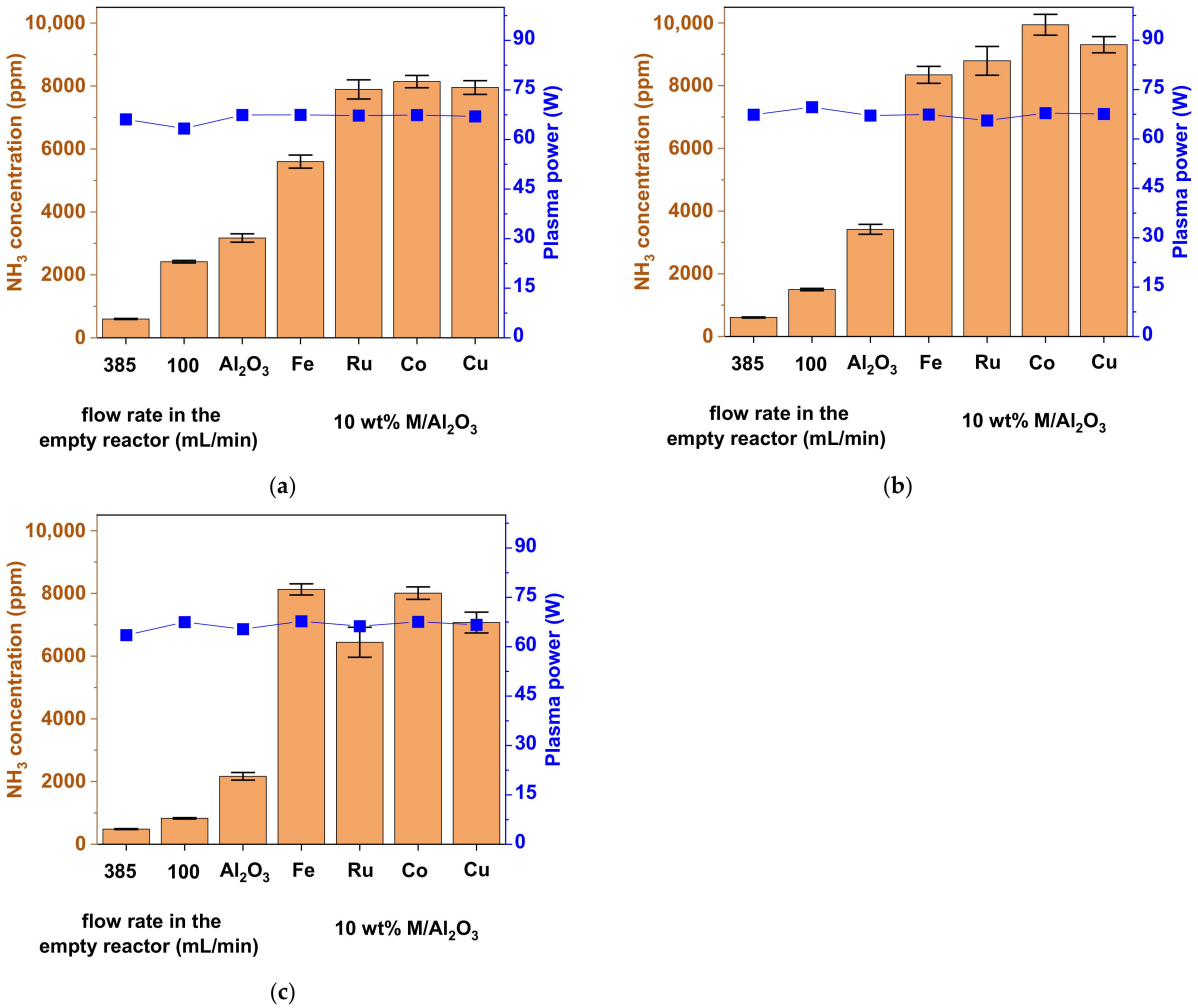

Figure 5. Concentration of NH_3 obtained from N_2 and H_2 in the plasma-catalytic reaction within the DBD reactor, for an empty reactor and a packed reactor with pristine Al_2O_3 beads, and Al_2O_3 beads impregnated with 10 wt% Fe, Ru, Co, or Cu catalyst. The empty reactor was used with two different feed gas flow rates: 385 and 100 mL/min, to have the same residence time and same mass flow rate, respectively, as the packed reactor. The experiments were performed with three H_2:N_2 ratios: (**a**) 3:1; (**b**) 1:1; (**c**) 1:3. The error bars denote the standard deviation between three independent experiments.

The performance of the catalysts was assessed for a total feed gas flow rate of 100 mL/min. Preliminary experiments showed that flow rates higher than 100 mL/min can cause a small decrease in EC (ca. 5% lower EC at a flow rate of 200 mL/min). At the same time, the reduced residence time due to the higher flow rate results in a dramatic decrease of the N_2 conversion and NH_3 yield. Therefore, in this work, we chose 100 mL/min as the flow rate, to ensure a reasonable concentration of NH_3 (around 1 vol%): we previously showed that the NH_3 production only becomes industrially feasible if the produced NH_3 concentrations are $\geq$1 vol% [16].

Besides the supported metal catalysts, we also performed plasma experiments with pristine Al_2O_3 beads, and in an empty reactor. The empty reactor experiments were done with two different feed gas flow rates: 100 mL/min and 385 mL/min. In terms of mass flow, the flow rate of 100 mL/min in the empty reactor is directly comparable to the packed bed experiments. However, because the plasma reactor was operated in a flow rather than a batch mode, the residence time of the gas within the plasma is affected due to the presence of the packing beads, and the plasma in the reactor extending outside the catalyst bed. The beads occupy most of the reactor volume, effectively reducing the volume through which the gas can pass. Hence, the residence time of the feed gas within the reactor, i.e., the time which the feed gas spends within the catalyst bed/plasma discharge region, is also reduced. In an approximation, a dense packing can be assumed, with the volume of the spheres occupying ca. 74% of the gap volume [53]. Therefore, the mass flow rate of 100 mL/min with the packing beads corresponds to the same residence time as a mass flow rate of 385 mL/min in the empty reactor. We acknowledge that the shape of the reactor and the catalyst bed may not allow perfectly dense packing. Besides, the residence time of the gas in the reactor is also affected by adsorption/desorption processes on the beads. Nonetheless, we believe that, in a first approximation, the two used mass flow rates (100 and 385 mL/min) present the so-called "envelope" conditions: the residence time of the gas in an empty reactor, which corresponds to the residence time of the gas in a packed reactor (operated at 100 mL/min), lies within these conditions. For clarity, in the case of the empty reactor, we refer to the flow rates of 100 mL/min and 385 mL/min as having "the same gas flow rate" and "the same residence time".

The results of the PC NH_3 experiments are shown in Figures 5 and 6. Besides the concentration of NH_3 (measured by NDIR; see Materials and Methods for details), we also evaluated the NH_3 production rate and energy consumption (EC) for the different catalysts and H_2:N_2 ratios: these two are the key factors in the evaluation of a process, which could be an alternative to the existing industrial technologies [14,16,26]. Here, the production rate and the EC were calculated as shown in Equations (2) and (3), respectively:

$$NH_3\ production\ rate\left(\frac{\text{mg}}{\text{h}}\right) = \frac{Mass\ flow\ rate_{NH_3}\left(\frac{\text{mL}}{\text{min}}\right) \times 17\left(\frac{\text{g}}{\text{mol}}\right)}{24\left(\frac{\text{L}}{\text{mol}}\right)} \times 60\left(\frac{\text{min}}{\text{h}}\right), \quad (2)$$

$$EC\left(\frac{\text{MJ}}{\text{mol}}\right) = \frac{Plasma\ power\ (\text{W})}{\frac{Mass\ flow\ rate_{NH_3}\left(\frac{\text{mL}}{\text{min}}\right)}{24\left(\frac{\text{L}}{\text{mol}}\right)\times 10^3\left(\frac{\text{mL}}{\text{L}}\right)\times 60\left(\frac{\text{s}}{\text{min}}\right)}} \times 10^{-6}\left(\frac{\text{MJ}}{\text{J}}\right), \quad (3)$$

where Mass flow rate(NH_3) is the partial flow rate (in mL/min) of NH_3 in the reaction mixture after the plasma reactor and is calculated as

$$Mass\ flow\ rate_{NH_3}\left(\frac{\text{mL}}{\text{min}}\right) = \frac{\left(Mass\ flow\ rate\ {}^{inlet}_{H_2} + Mass\ flow\ rate\ {}^{inlet}_{N_2}\right)\left(\frac{\text{mL}}{\text{min}}\right) \times \frac{C_{NH_3}\ (\text{ppm})}{10^6}}{1 + \frac{C_{NH_3}\ (\text{ppm})}{10^6}} \quad (4)$$

to account for gas contraction due to the stoichiometry of formation of NH_3 from H_2 and N_2.

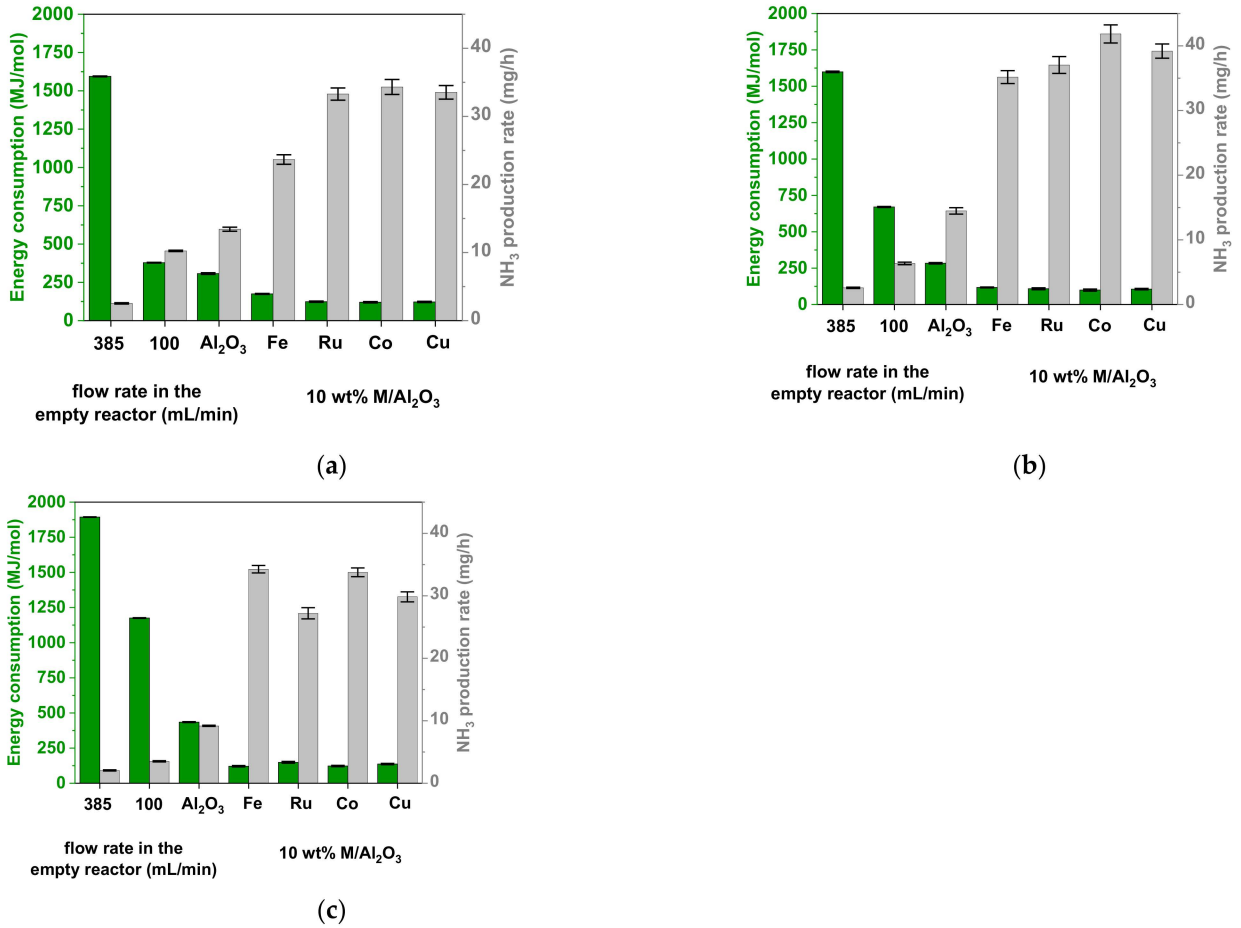

Figure 6. Energy consumption of NH_3 formation (left y-axis) and NH_3 production rate (right y-axis), obtained from N_2 and H_2 in the plasma-catalytic reaction within the DBD reactor, for an empty reactor and a packed reactor with pristine Al_2O_3 beads, and Al_2O_3 beads impregnated with 10 wt% Fe, Ru, Co, or Cu catalyst. The empty reactor was used with two different feed gas flow rates: 385 and 100 mL/min, to have the same residence time and same mass flow rate, respectively, as the packed reactor. The experiments were performed with three H_2:N_2 ratios: (**a**) 3:1; (**b**) 1:1; (**c**) 1:3. The error bars denote the standard deviation between three independent experiments.

When the empty reactor was used, the concentrations of the produced NH_3 were extremely low with all three used H_2:N_2 ratios. For the empty reactor experiments with the same apparent gas residence time as the reactor packed with beads, the maximal concentration of NH_3 did not exceed 600 ppm, while, under conditions with the same gas flow rate as the packed reactor, it reached a maximum of ca. 2400 ppm, for the 3:1 H_2:N_2 ratio (Figure 5). These low values resulted in very high ECs, with the minimal one being around 300 MJ/mol, again, for the 3:1 H_2:N_2 ratio (Figure 6a). Under these conditions, the production rate of NH_3 was also expectedly low, ca. 10 mg/h at maximum. The other H_2:N_2 ratios gave even lower NH_3 concentrations and production rates, as well as much higher ECs.

When the Al_2O_3 beads were introduced into the reactor, we observed a prominent increase in NH_3 concentration and production rate and a respective decrease in EC compared to the empty reactor (even with the same flow rate). This was especially the case for the 1:1 H_2:N_2 ratio, where the EC decreased, and the NH_3 production rate increased, by a factor of ca. 2.5, to values of 280 MJ/mol and 15 mg/h, respectively (compared to 670 MJ/mol and 6 mg/h with the empty reactor for the same mass flow rate). In practice, the addition of beads induces two effects. Firstly, the almost exclusively gas phase reactions (in the empty reactor) become largely, or even predominantly, reactions involving the surface species, regardless of whether the reaction progresses via the Langmuir-Hinshelwood,

or the Eley-Rideal [43] mechanism, as mentioned above. Secondly, the packing beads change the dielectric properties of the whole reactor. This results in an increased local electric field [54] and, thus, a higher electron energy and more efficient inelastic collisions, ultimately producing higher NH_3 yields and lower EC.

When the 10 wt% M/Al_2O_3 catalysts were used, the production of NH_3 increased even more. As in thermal catalysis, this may be ascribed to the presence of active metals, which could: (i) lead to additional adsorption sites for the reactive species, resulting in a local increase of their concentration; and (ii) facilitate the dissociative adsorption of N_2. Among the four screened supported metal catalysts, no dramatic differences were observed in terms of the NH_3 concentration and production rate. The values of EC. varied in the range between 99 MJ/mol (Co; Figure 6b) to around 120 MJ/mol for all other catalyst and conditions, with the exception of 10 wt% Fe/Al_2O_3 at the 3:1 H_2:N_2 ratio, where it was 174 MJ/mol (Figure 6a). Overall, the 10 wt% Co/Al_2O_3 catalyst performed slightly better than Fe, Ru, and Cu. Here, the maximal values of NH_3 concentration and production rate reached ca. 10000 ppm (or 1 vol%) and 42 mg/h, respectively, at the 1:1 H_2:N_2 ratio, which corresponded to the minimal achieved EC of 99 MJ/mol (Figures 5b and 6b).

An important finding here was that, under all conditions with packing beads (pristine Al_2O_3, and 10 wt% M/Al_2O_3 for all catalysts), the best results were not obtained with the stoichiometric ratio 3:1 of H_2:N_2 (such as with an empty reactor, where nearly all reactions occur homogeneously in the gas phase) but instead 1:1. The shift towards the optimal ratio 1:1 could be due to the 'competition' between H_2 and N_2 molecules for active sites on the catalyst surface of the beads. Therefore, a higher N_2 fraction would favour the production of NH_3, especially because the dissociation energy of N_2 (9.76 eV) is higher than that of H_2 (4.48 eV), making the activation of N_2 the rate-determining step [19]. Although N_2 molecules can also be activated by vibrational or electronic excitation [25,26,55], a higher relative amount of N_2 would still result in a larger number of excited N_2 molecules. On the other hand, an even lower H_2:N_2 ratio (e.g., 1:3) would result in a smaller number of plasma-excited H_2 molecules and, hence, a lower NH_3 formation. Besides, a high H_2:N_2 ratio (3:1) could lead to the excess of plasma-excited hydrogen species, which facilitate the decomposition of NH_3 [19,39].

We need to mention, however, the speculative nature of this discussion. The available literature contrastingly reports empirical data which describe this effect [32], as well as the opposite ones, i.e., the H_2:N_2 ratios optimal for NH_3 production by plasma catalysis being, e.g., 3:1 [56] or 1:4 [35]. Therefore, the optimal H_2:N_2 ratio likely depends on the experimental conditions, e.g., reactor geometry, plasma power, temperature, parameters, type of the catalyst bed, etc.

2.3. TOFs and Implications with Respect to Reaction Mechanisms

For the comparison of the catalyst performance and validation of the microkinetic model predictions [43], we calculated the TOFs on 10 wt% Al_2O_3-supported Fe, Ru, Co and Cu catalysts at the H_2:N_2 gas ratios of 3:1, 1:1, and 1:3. The TOFs were calculated using the following formula:

$$TOF\left(s^{-1}\right) = \frac{Rate_{M/Al_2O_3}\left(\frac{mol}{s}\right) - Rate_{Al_2O_3}\left(\frac{mol}{s}\right)}{Quantity\ of\ metal\ adsorption\ sites\ (mol)} = \frac{Rate_{M/Al_2O_3}\left(\frac{mol}{s}\right) - Rate_{Al_2O_3}\left(\frac{mol}{s}\right)}{Metal\ surface\ area\ (m^2) \times Site\ density\ \left(\frac{mol}{m^2}\right)}, \quad (5)$$

for which we used the NH_3 production rate data presented in Figure 6. The metal surface area was defined as the fraction of the total catalyst surface (total catalyst surface × metal coverage; Tables 1 and 3). The total catalyst surface was calculated from S_{BET} × amount of catalyst (in g), with the assumption of similar physisorption of N_2 by both metal sites and Al_2O_3 sites:

$$Metal\ surface\ area\ \left(m^2\right) = S_{BET}\left(\frac{m^2}{g}\right) \times m_{beads}\ (g) \times Metal\ coverage. \quad (6)$$

Lastly, the obtained metal surface area was multiplied by the site density (number of sites per square meter), for which we assumed an estimated theoretical value of 10^{19} sites/m^2 (which is generally representative of metal surfaces and used for calculations [28,57]). This corresponds to 1.66×10^{-5} mol/m^2, as used in Equation (5).

NH_3 production is not only determined by the amount of catalyst loaded onto the Al_2O_3 beads. A different dispersion of the metal particles can change the active surface area and, thus, the catalytic reaction rate. For a correct comparison of the metal catalyst activity, therefore, it is important to compare the process TOFs. As formulated in Equation (5), in the defined TOFs we subtracted the values of the background NH_3 produced in the gas phase, over the Al_2O_3 beads and at the electrodes (denoted together as Rate(Al_2O_3) in Equation (5)), and only account for the production at the active metal surface area. This allows comparing the unique contributions of each metal catalyst separately.

We found that the highest TOFs correspond to reactions with the 10 wt% Ru/Al_2O_3 and Cu/Al_2O_3. In general, for any of the studied H_2:N_2 ratios in the feed gas, the TOF values were in the following order: Fe < Co < Ru < Cu. As also seen from the data shown in Figures 5 and 6, the 1:1 gas ratio showed slightly higher TOFs than the other gas ratios. However, the most important result is not the actual value or even a numerical trend of TOF between the catalysts, but the fact that the calculated TOFs are all in roughly the same order of magnitude for each of three feed gas ratios (Figure 7). In other words, although some differences between metals are apparent, no discernible chemical trend of a "volcano" type (which is mostly plotted on a log scale) is observed.

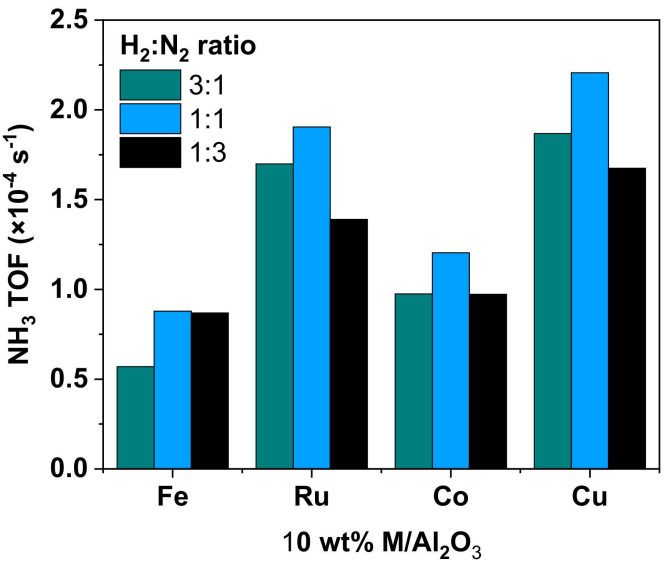

Figure 7. Calculated TOF values in PC NH_3 synthesis with the 10 wt% $A_{l2}O_3$-supported Fe, Ru, Co, and Cu catalysts in the DBD reactor. The TOFs were calculated for the three H_2:N_2 ratios: 3:1; 1:1; and 1:3.

3. Discussion

We studied the chemical activity of four different transition metal catalysts (10 wt% Fe, Ru, Co, and Cu on Al_2O_3 beads) for plasma-catalytic NH_3 synthesis.

In terms of plasma performance, our results with 10 wt% Co/Al_2O_3 and 1:1 ratio of H_2:N_2 showed the lowest EC of 99 MJ/mol, corresponding to an NH_3 yield of 1% (calculated as shown in Equation (7)) and a production rate of 42 mg/h (Figures 5b and 6b), which is of preparative interest.

$$NH_3\ yield(\%) = N_2\ conversion\ (\%) = \frac{\frac{1}{2}\ Mass\ flow\ rate_{NH_3}\left(\frac{\mathrm{mL}}{\mathrm{min}}\right)}{Mass\ flow\ rate\ {}^{inlet}_{N_2}\left(\frac{\mathrm{mL}}{\mathrm{min}}\right)} \times 100\%. \quad (7)$$

Table 4 gives a comparative overview of the results of PC NH_3 synthesis reported in literature, with a focus on the best EC values in each work: indeed, the EC remains the main characteristic of a process by which its competitiveness with HB is evaluated [26]. We compare the values of NH_3 yield and not NH_3 concentration due to the availability of the data in the source works. Of course, the yield and the concentration of NH_3 are directly related as shown in Equations (4) and (7). While other works report lower EC values, the respective NH_3 yields are often also very low (from <0.1 to 0.7%) and correspond to similarly low values of NH_3 concentrations (<1 vol%), as seen e.g., in [18,35,46,56] In our previous work, we demonstrated that a process of NH_3 production becomes plausible only if the NH_3 concentration in the reaction mixture is ≥1 vol% due to the 'hidden' additional energy costs required for product separation [16]. In this regard, our value of ca. 1 vol% (or 10,000 ppm; see Figure 5) falls within the desired range. Furthermore, in some of the listed works, the overall PC NH_3 production efficiency was due to the combination of thermal catalysis and plasma catalysis [35]. In our study, the temperature was substantially lower (<120 °C), suggesting that the contribution of thermal catalytic effects was likely negligible. However, it must be noted that the reactive system here was not specifically optimised due to the fundamental nature of this study. Moreover, the amount of catalyst used in this work (12 g) was chosen to fill the volume in the reactor corresponding to the discharge region between the two electrodes (see Materials and Methods). In any case, the production rate of NH_3 (in $mg/(h \times g_{cat})$ obtained in this study was in the range of those reported in literature (see Table S2 in Supplementary Materials for details). Further work including optimisation of the reactor design geometry, as well as plasma properties and operating conditions (e.g., power, frequency, feed gas flow rate), can likely lead to lower EC.

Table 4. Summary of studies on NH_3 production from N_2 and H_2 in DBD plasma reactors, as well as comparison with our work.

Source [1]	Catalyst	T (°C)	Plasma Power (W)	H_2:N_2 Ratio	Energy Consumption (MJ/mol)	N_2 Conversion/ /NH_3 Yield (%)	NH_3 Production Rate (mg/h)
[30]	Ru/Al_2O_3	20	127	3:1	244	2.4	16
[31]	PZT	50	n/a [2]	3:1	68	2.7	12
[32]	Cu	n/a	n/a	1:1	19	1.4	71
[58]	DLC-coated Al_2O_3	160	70	3:1	350	n/a	12
[59]	Ru-Cs-K-Ba/ /Si-MCM-41	150	n/a	1:1	36	<0.1	n/a
[35]	RuO-MgO/Al_2O_3	300	4	1:4	2	<0.1	119
[36]	Ni/SiO_2 + $BaTiO_3$	140	87	3:1	81	12.0	32
[33]	Au	n/a	100	1:1	79	2.5	77
[42]	Co/Al_2O_3	200	10	2:1	36	1.0	17
[38]	Ni/Al_2O_3	35	10	2:1	56	0.7	10
[37]	Co/Al_2O_3	200	10	1:3	102	0.1	6
[60]	Ni-MOF-74	n/a	50	4:1	265	n/a	22
[39]	Ru/Al_2O_3	118	38	1:2	32	1.1	76
[46]	Ru/MgO	200	26	1:2	47	0.1	25

Table 4. *Cont.*

Source [1]	Catalyst	T (°C)	Plasma Power (W)	H_2:N_2 Ratio	Energy Consumption (MJ/mol)	N_2 Conversion/ /NH_3 Yield (%)	NH_3 Production Rate (mg/h)
[56]	alkaline Al_2O_3	>105	n/a	3:1	9	<0.1	7
[61]	SiO_2	440	n/a	1:2	50	0.2	60
[19]	Rh/Al_2O_3	325	n/a	1:2	65	1.1	29
[62]	Ru/C	n/a	13	3:1	85	0.5	10
[18]	Ru-K/MgO	325	4	1:1	46	0.6	5
this work	Co/Al_2O_3	<120	67	1:1	99	1.0	42

[1] The catalysts, experimental details, and the calculated values of NH_3 production and N_2 conversion correspond to the lowest energy consumption (EC) reported in the respective publication. [2] Not available: the data were absent, and the absence of the necessary experimental details did not allow us to calculate the numerical values.

We also compared the performance of the four used metals: Ru as optimal for thermal catalysis, Fe as mostly used in the industrial HB process, Co as predicted to be optimal in the case of vibrational excitation reactions, and Cu as predicted to be active only in the case of radical reactions. For this, we calculated the TOFs for three gas phase ratios, 3:1, 1:1, and 1:3 H_2:N_2. As opposed to thermal catalysis expectations, the obtained results do not showcase any particular chemical trend and the performance of the different transition metals is remarkably similar. The observed TOFs only show random deviations that cannot be explained by thermal activity of the catalysts or chemical activity of vibrationally excited molecules, as predicted by previous works [42,43].

Under thermal conditions, the metal performance follows the Sabatier principle, which gives rise to so-called "volcano"-behaviour. For NH_3 synthesis the top of the volcano (i.e., the best performance) lies in between Fe and Ru, and the catalyst activity drops steeply (exponentially) on both the noble and the non-noble side of the volcano [42]. By means of microkinetic modelling, Mehta et al. predicted that, in plasma catalysis, the peak of the TOF volcano would shift towards more noble catalysts (with a maximum around Ni and Co) due to interactions of the transition metal with vibrationally excited N_2 [42]. However, their model still predicted the same steep slopes on both flanks of the volcano and, thus, could not explain why Fe, Ru, and Cu perform virtually equally well (and in the cases of Ru and Cu, even better).

We have previously studied possible effects of plasma-generated radicals by extending the Mehta model with radical adsorption and Eley-Rideal reactions, and adopting plasma phase densities of radicals and vibrational distribution functions from plasma kinetics models [28,43]. We calculated the NH_3 TOFs from microkinetic modelling of an H_2/N_2 plasma in contact with various transition metal catalysts, at 400 K and 1 bar, which are typical operating conditions for a DBD (including the setup presented in this work). Kinetic input data was based on scaling relations obtained from DFT to allow a large screening of the activity of different transition metal catalysts. The conclusion of the computational work was that these unique reactions have the potential to break the Sabatier principle and render the "volcano" trend inapplicable, as appears to be the case (Figure 8).

The fact that the NH_3 concentrations seem to be largely independent from the actual transition metal used might be explained by the contributions of plasma-generated radicals interacting with the metal surface [43]. While vibrational excitations of N_2 are expected to increase the performance of catalysts, such as Co and Ni (which are slightly more noble than the thermally optimal Ru), they cannot explain a similarity in performance between them and the Cu catalyst, nor the Fe and Ru catalysts. The computational results suggested that radical adsorption reactions could significantly activate the noble catalysts (e.g., Cu), while ER reactions are expected to activate the non-noble catalysts (e.g., Fe). Therefore,

under such conditions, the thermally observed "volcano" behaviour would be cancelled and the transition metals would behave similarly. At the same time, the equal performance of the different transition metals cannot be explained by homogeneous plasma reactions, reactions at the reactor walls, or activity of the support because the empty reactor and the reactor filled with pure Al_2O_3 beads perform significantly worse (Figures 5 and 6). Additionally, the TOFs reported in Figure 8 exclude the contribution of background NH_3 synthesis, proving the activity of each metal under plasma-catalytic conditions.

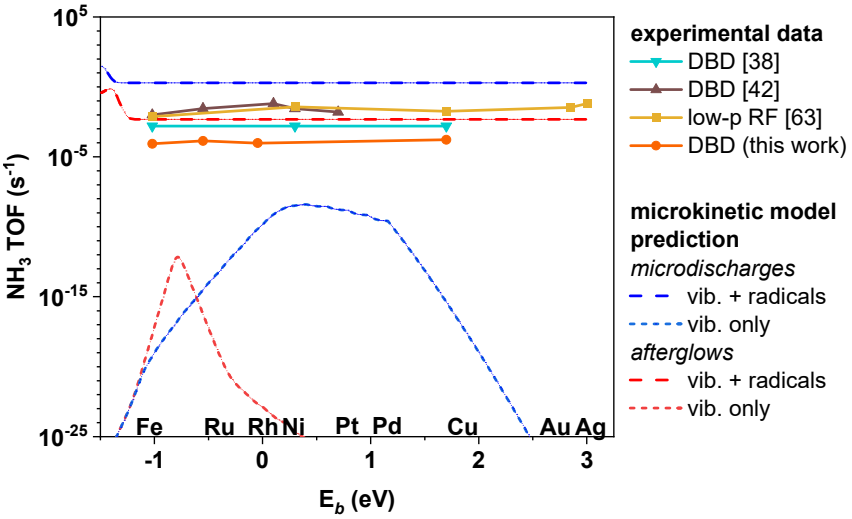

Figure 8. Comparison between the NH_3 TOF values obtained in our experiments, as well as in literature, and predicted by the microkinetic computational model (described in detail elsewhere [43]). TOFs are showcased as a function of the N* binding energy on the metal terrace sites.

We want to highlight that catalyst activities are expected to differ by several orders of magnitude in thermal catalysis and in plasma catalysis, if they are governed by vibrational excitations. However, the results presented here and the results reported in previous experimental works showcase much smaller deviations. We compiled the results from other experimental works, together with our own data, and compare them with the trends predicted computationally [43], as shown in Figure 8. We plotted the results with the 1:3 H_2:N_2 ratio from our experiments because it compares best with the data from other works which used high N_2 contents. In any case, the difference between the results obtained with the 3:1, 1:1, and 1:3 H_2:N_2 ratios in our work is very small when put on a logarithmic scale. Besides the two works by Wang et al. [38] and Mehta et al. [42] describing the performance of different catalytic metals in DBD reactors, we also added a dataset obtained by Shah et al. in a low-pressure radiofrequency plasma [63], which interestingly exhibited the same properties (i.e., the absence of the "volcano" trend), thus indirectly suggesting that the implications of our model may reach beyond atmospheric pressure plasma conditions.

We specifically note that this comparison is aimed merely at highlighting the qualitative trends of TOFs as a function of the catalyst material. A quantitative comparison between observed and calculated TOFs is beyond the level of detail that computational modelling can provide.

We acknowledge that a DBD can perform both in a filamentary and uniform regime [28,38]. However, it is most commonly filamentary (i.e., consisting of microdischarges and their afterflows). Therefore, the modelling results in Figure 8 are shown for both the microdischarges and their afterglows of a filamentary plasma. For both conditions, results were calculated for a plasma phase containing vibrationally excited N_2 and plasma-generated radicals, as well as a plasma phase containing only vibrationally excited N_2 (denoted "vib. only" in the legend of Figure 8).

The comparison of the experimental trends and the modelling results clearly shows that the experimental data align much better with the model results containing radical

reactions than with the model results accounting only for vibrational excitation. It is clear that none of the experiments showcase true "volcano" behaviour (which would be predicted by the reaction pathways from vibrational excitation only, as illustrated in Figure 8). Instead, they exhibit the same trend as our calculated TOFs with the full model, including the effect of radicals and ER reactions. Each of the experimental works predicts certain catalyst materials to perform slightly better than others, but the differences are small, and no consistent chemical differences are noticeable.

While this comparison does not provide definitive conclusions on reaction mechanisms, it strongly suggests the potential contribution of radical adsorption and ER reactions (rather than LH reactions) in PC NH_3 synthesis.

4. Materials and Methods

4.1. Preparation of Catalyst Beads

Al_2O_3-supported catalysts were prepared as follows. Metal precursors were purchased from Sigma-Aldrich (St. Louis, MO, USA): $Co(NO_3)_2{\cdot}6H_2O$ (99.5%), $Cu(NO_3)_2{\cdot}3H_2O$ ($\geq$99%), $Fe(NO_3)_3{\cdot}9H_2O$ (99.5%), $RuCl_3{\cdot}xH_2O$ (40 wt% Ru). The supported metal catalysts were prepared using γ-Al_2O_3 beads supplied by Gongyi Tenglong Water Treatment Material Co. Ltd., Gongyi, China (>99%) with a diameter 1.4–1.8 mm, based on literature [38]. Al_2O_3 beads were first calcined at 400 °C in a muffle furnace (Lenton ECF 12/6) in air for 3 h, and let cool down. Then, a solution of the respective metal precursor in de-ionised water was used for incipient wetness impregnation of the γ-Al_2O_3 beads. For this, a solution of a respective salt was slowly added to the beads until full absorption of liquid. The volume of solution (0.75 mL per 1 g of beads) was chosen empirically as the maximal volume adsorbed by the beads. Further, the beads were left drying at room temperature for 12 h, then dried at 120 °C in a drying oven (Memmert UF55, Schwabach, Germany) for 8 h, and, finally, calcined in air at 540 °C for 6 h. Before plasma experiments, the catalysts were reduced in plasma operated with an Ar/H_2 gas mixture (1:1) for 8 h [44]. The amounts and concentrations of the precursor solutions were calculated so that the amount of the adsorbed metal salt would correspond to a 10 wt% loading of the respective metals.

4.2. Catalyst Characterisation

The specific surface area of the samples was measured using a nitrogen adsorption-desorption technique (Micromeritics TriStar II, Norcross, GA, USA) at −196 °C. Before the measurement, the samples (0.1500 g) were degassed at 350 °C for 4 h. The surface area was calculated based on the Brunauer–Emmett–Teller (BET) approach. The total pore volume of the samples was measured at a relative pressure (P/P_0) of 0.99.

The structural properties of the samples were investigated by XRPD, conducted using a Rigaku SmartLab 9 kW diffractometer (Tokyo, Japan) with Cu Kα radiation (240 kV, 50 mA). The samples were scanned from 5° to 80° at a step of 0.01° with the scanning speed of 10 °/min. The catalyst beads were powderised prior to analysis.

The metal loading was measured using energy-dispersive X-ray spectroscopy (EDX) in a Quanta 250 FEG scanning electron microscope (Hillsboro, OR, USA) operated at 30 kV.

The size distribution of the metal particles was measured by high-angle annular dark-field scanning transmission electron microscopy (HAADF-STEM) using a Thermo Fischer Scientific Osiris TEM (Waltham, MA, USA) operated at 200 kV. Prior to the measurements, the specimens were crushed and suspended in ethanol and then drop-cast onto the TEM grid. An in-house made molybdenum holey carbon grid was used in the analysis.

4.3. Plasma Setup

The feed gas flow (H_2 and N_2, total flow rate 100 mL/min) was supplied using mass flow controllers (Bronkhorst, Ruurlo, The Netherlands) connected to H_2 and N_2 gas cylinders (both 99.999%, Praxair, Danbury, CT, USA). The feed gases H_2 and N_2 were mixed using a T-connector, and subsequently introduced into the DBD plasma reactor shown in Figure 9. The cylindrical DBD reactor consisted of an inner ground electrode (stainless

steel rod, diameter 8 mm) surrounded by a hollow ceramic cylinder (dielectric barrier) with an inner diameter 17 mm and outer diameter 22 mm. Both ends of the reactor were held in place with stainless steel caps, which were also connected to the inner electrode (Figure 9). The outer electrode (stainless steel mesh, 100 mm length, thickness ca. 1 mm) was positioned around the outer walls of the ceramic cylinder. As a result, the inner (ground) electrode and the outer (high voltage) electrode were separated by a ceramic cylinder with a wall thickness of 2.5 mm, and a gap of ca. 4.5 mm. This gap was filled with catalyst beads (12 g, ca. 20 mL volume), held on both sides with glass wool.

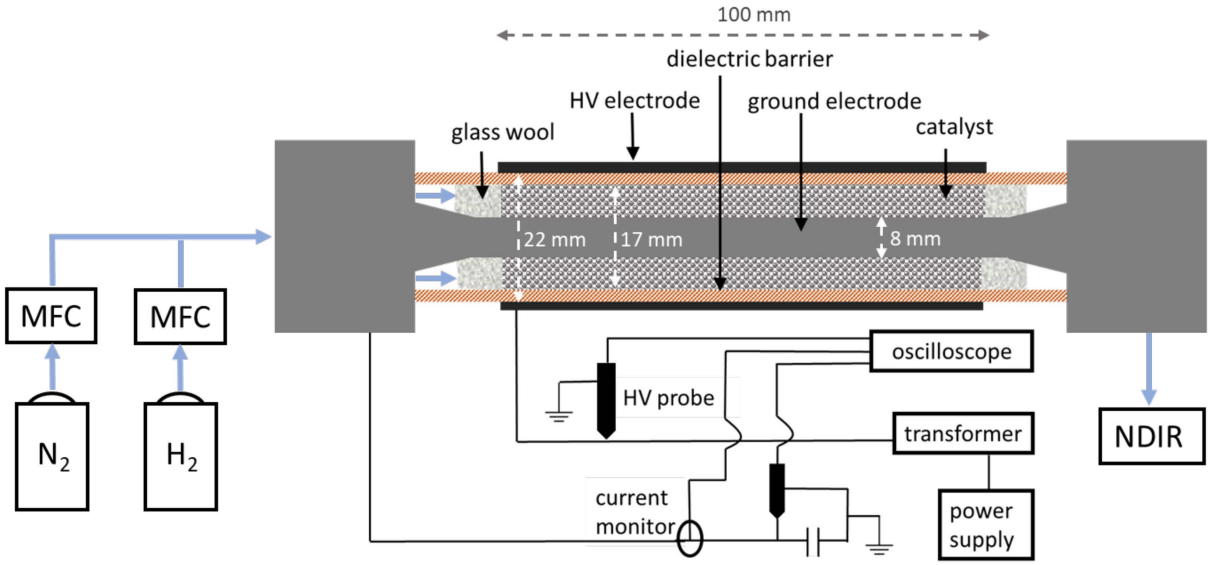

Figure 9. Schematic representation of the DBD plasma reactor for plasma-catalytic NH_3 synthesis.

The reactor was positioned on a plastic support inside a grounded Faraday cage. No additional insulation was applied to the reactor.

The discharge was driven by a high frequency power supply unit (PSU) AFS G10S-V (AFS GmbH, Delmenhorst, Germany) connected to a transformer. The electrical characteristics were monitored with a digital oscilloscope (Pico Technology PicoScope 6402D, St. Neots, UK) using a high voltage probe (Tektronix P6015A, Beaverton, OR, USA), and a current monitor (Pearson Electronics Inc. 4100, Palo Alto, CA, USA). An additional voltage probe was connected to an external capacitor to obtain the Lissajous figures. The PSU was operated at a frequency of 23.5 kHz, and a power of 100 W. The set PSU power of 100 W allowed a power deposition into the plasma of ca. 65 W, as calculated from the Lissajous figures obtained from the current and voltage parameters. The temperature of the outer walls of the ceramic tube was 104 °C, as measured with a thermocouple connected to a temperature data logger (RS Pro 1384, Corby, UK). The temperature of the gas inside the reactor was calculated to be around 108 °C using a computational model described elsewhere [64]. We acknowledge that the values obtained this way are only approximate, although a large difference with the computational results is unlikely. In any case, we report the temperature here being <120 °C for simplicity.

The concentration of the produced NH_3 in the gas outlet from the DBD reactor was analysed with a non-dispersive infrared (NDIR) sensor (Emerson, Rosemount^{TM} X-stream Enhanced XEGP Continuous Gas Analyzer, St. Louis, MO, USA). The quantitative analysis was performed when the concentration of NH_3 reached a steady-like state, i.e., did not vary by more than 100–200 ppm within a period of at least 15 min. The NDIR was calibrated using a calibration gas (4.89 vol% NH_3 in He) purchased from Praxair.

Each experiment was conducted in triplicate. The error bars on the graphs show a standard deviation between the three obtained values.

5. Conclusions

In this work, we explored the relative activity of four different Al_2O_3-supported transition metal catalysts (Fe, Ru, Co, and Cu) in plasma-catalytic NH_3 synthesis. Our experimental results showed some difference between catalyst activity, albeit incremental: no classic "volcano" plot of metal activity (typical in thermal catalysis) was observed. When compared to the predictions obtained by a computational model, the obtained data indicate a good agreement with the calculations based on the interactions of radicals rather than vibrationally excited molecules. Specifically, this good agreement indicates the importance of radical adsorption reactions and Eley-Rideal reaction mechanisms in plasma-catalytic NH_3 synthesis. The relative indifference of the nature of the transition metal to be used as catalyst suggests that cheaper and more abundant metals are quite feasible for this process, which naturally increases the overall cost-effectiveness. Although not absolutely definitive, these insights can help in developing cheaper catalysts for the plasma-catalytic synthesis of NH_3.

Certainly, plasma-based processes of NH_3 production are not fully capable of replacing the large-scale centralised production facilities, such as those used in the Haber-Bosch process. However, this is also an advantage of plasma technology: it can be operated on a small scale for decentralisation [26]. Small scale plasma reactors are compliant with the policies seeking to make the production of essential chemicals more benign by being able to operate on renewable electricity [13], and allowing production of fertilisers on site, thus reducing the transport costs and increasing the fertiliser availability in remote areas [65,66]. Therefore, plasma-catalytic NH_3 synthesis is an indispensable auxiliary technology in the world-wide fertiliser production.

Supplementary Materials: The following are available online at https://www.mdpi.com/article/10.3390/catal11101230/s1, Figure S1. XRD diffractogram of the catalysts used in our work; Table S1: Measured active surface area and pore volume for the 10 wt% Co/Al_2O_3 catalyst before (fresh) and after (spent) the plasma-catalytic NH_3 synthesis experiments, Figure S2: SEM-EDX images of the 10 wt% M/Al_2O_3 catalysts with EDX maps applied for visualisation of the respective metals, Figure S3. Current and voltage waveforms for the plasma-catalytic NH_3 synthesis experiments with different Al_2O_3-supported catalysts and pristine Al_2O_3, at different H_2:N_2 ratios in the feed gas, Figure S4. Lissajous figures for the plasma-catalytic NH_3 synthesis experiments with different Al_2O_3-supported catalysts and pristine Al_2O_3, at different H_2:N_2 ratios in the feed gas; Table S2. The amount of the used catalyst, and the production rate of NH_3 (in $mg/(h \times g_{cat})$ in our work compared to literature reports.

Author Contributions: Conceptualisation, Y.G., Y.E. and A.B.; methodology, Y.G., E.V. and Y.Y.; formal analysis, Y.G., Y.E., E.V., C.N. and Y.Y.; investigation, Y.G., Y.E., K.v.V., E.V. and Y.Y.; resources, Y.Y., S.B. and A.B.; data curation, Y.G., E.V. and Y.Y.; writing—original draft preparation, Y.G., E.V., Y.E., K.v.V. and C.N.; writing—review and editing, Y.G., E.V., Y.E., K.v.V., S.B. and A.B.; visualisation, Y.G. and E.V.; supervision, S.B. and A.B.; project administration, A.B.; funding acquisition, S.B. and A.B. All authors have read and agreed to the published version of the manuscript.

Funding: This research was funded by the Catalisti Moonshot project P2C, the European Research Council (ERC) under the European Union's Horizon 2020 research and innovation programme (ERC Synergy Grant 810182 SCOPE, and ERC Consolidator Grant 815128 REAL-NANO), the Excellence of Science FWO-FNRS project (FWO grant ID GoF9618n, EOS ID 30505023), and the Methusalem project of the University of Antwerp.

Data Availability Statement: The data presented in this study are available in the article itself and the Supplementary Materials (SI). Detailed data are available on request from the corresponding author.

Acknowledgments: The authors thank Joshua Boothroyd (PLASMANT) for his help with the quantitative temperature assessment.

Conflicts of Interest: The authors declare no conflict of interest.

References

1. Erisman, J.W.; Sutton, M.A.; Galloway, J.; Klimont, Z.; Winiwarter, W. How a century of ammonia synthesis changed the world. *Nat. Geosci.* **2008**, *1*, 636–639. [CrossRef]
2. Hoffman, B.M.; Lukoyanov, D.; Yang, Z.-Y.; Dean, D.R.; Seefeldt, L.C. Mechanism of nitrogen fixation by nitrogenase: The next stage. *Chem. Rev.* **2014**, *114*, 4041–4062. [CrossRef] [PubMed]
3. Sun, J.; Alam, D.; Daiyan, R.; Masood, H.; Zhang, T.; Zhou, R.; Cullen, P.J.; Lovell, E.C.; Jalili, A.; Amal, R. A hybrid plasma electrocatalytic process for sustainable ammonia production. *Energy Environ. Sci.* **2021**, *14*, 865–872. [CrossRef]
4. Wang, M.; Khan, M.A.; Mohsin, I.; Wicks, J.; Ip, A.H.; Sumon, K.Z.; Dinh, C.-T.; Sargent, E.H.; Gates, I.D.; Kibria, M.G. Can sustainable ammonia synthesis pathways compete with fossil-fuel based Haber-Bosch processes? *Energy Environ. Sci.* **2021**, *14*, 2535–2548. [CrossRef]
5. Smith, C.; Hill, A.K.; Torrente-Murciano, L. Current and future role of Haber-Bosch ammonia in a carbon-free energy landscape. *Energy Environ. Sci.* **2020**, *13*, 331–344. [CrossRef]
6. Kobayashi, H.; Hayakawa, A.; Somarathne, K.K.A.; Okafor, E.C. Science and technology of ammonia combustion. *Proc. Combust. Inst.* **2019**, *37*, 109–133. [CrossRef]
7. Nayak-Luke, R.M.; Bañares-Alcántara, R. Techno-economic viability of islanded green ammonia as a carbon-free energy vector and as a substitute for conventional production. *Energy Environ. Sci.* **2020**, *13*, 2957–2966. [CrossRef]
8. Kyriakou, V.; Garagounis, I.; Vourros, A.; Vasileiou, E.; Stoukides, M. An electrochemical Haber-Bosch process. *Joule* **2020**, *4*, 142–158. [CrossRef]
9. Pfromm, P.H. Towards sustainable agriculture: Fossil-free ammonia. *J. Renew. Sustain. Energy* **2017**, *9*, 034702. [CrossRef]
10. Cui, X.; Tang, C.; Zhang, Q. A review of electrocatalytic reduction of dinitrogen to ammonia under ambient conditions. *Adv. Energ. Mater.* **2018**, *8*, 1800369. [CrossRef]
11. Hargreaves, J.S.J.; Chung, Y.-M.; Ahn, W.-S.; Hisatomi, T.; Domen, K.; Kung, M.C.; Kung, H.H. Minimizing energy demand and environmental impact for sustainable NH_3 and H_2O_2 production—A perspective on contributions from thermal, electro-, and photo-catalysis. *Appl. Catal. A Gen.* **2020**, *594*, 117419. [CrossRef]
12. Chen, J.G.; Crooks, R.M.; Seefeldt, L.C.; Bren, K.L.; Bullock, R.M.; Darensbourg, M.Y.; Holland, P.L.; Hoffman, B.; Janik, M.J.; Jones, A.K.; et al. Beyond fossil fuel-driven nitrogen transformations. *Science* **2018**, *360*, 6391. [CrossRef] [PubMed]
13. Bogaerts, A.; Neyts, E.C. Plasma technology: An emerging technology for energy storage. *ACS Energy Lett.* **2018**, *3*, 1013–1027. [CrossRef]
14. Rouwenhorst, K.H.R.; Jardali, F.; Bogaerts, A.; Lefferts, L. From the birkeland-eyde process towards energy-efficient plasma-based NO_x synthesis: A techno-economic analysis. *Energy Environ. Sci.* **2021**, *14*, 2520–2534. [CrossRef]
15. Gorbanev, Y.; Privat-Maldonado, A.; Bogaerts, A. Analysis of short-lived reactive species in plasma-air-water systems: The dos and the do nots. *Anal. Chem.* **2018**, *90*, 13151–13158. [CrossRef]
16. Hollevoet, L.; Jardali, F.; Gorbanev, Y.; Creel, J.; Bogaerts, A.; Martens, J.A. Towards green ammonia synthesis through plasma-driven nitrogen oxidation and catalytic reduction. *Angew. Chem. Int. Ed.* **2020**, *59*, 23825–23829. [CrossRef]
17. Li, L.; Tang, C.; Cui, X.; Zheng, Y.; Wang, X.; Xu, H.; Zhang, S.; Shao, T.; Davey, K.; Qiao, S.-Z. Efficient nitrogen fixation to ammonia through integration of plasma oxidation with electrocatalytic reduction. *Angew. Chem. Int. Ed.* **2021**, *60*, 14131–14137. [CrossRef]
18. Rouwenhorst, K.H.R.; Burbach, H.G.B.; Vogel, D.W.; Núñez Paulí, J.; Geerdink, B.; Lefferts, L. Plasma-catalytic ammonia synthesis beyond thermal equilibrium on Ru-based catalysts in non-thermal plasma. *Catal. Sci. Technol.* **2021**, *11*, 2834–2843. [CrossRef]
19. Patil, B.S.; Cherkasov, N.; Srinath, N.V.; Lang, J.; Ibhadon, A.O.; Wang, Q.; Hessel, V. The role of heterogeneous catalysts in the plasma-catalytic ammonia synthesis. *Catal. Today* **2021**, *362*, 2–10. [CrossRef]
20. Gorbanev, Y.; Vervloessem, E.; Nikiforov, A.; Bogaerts, A. Nitrogen fixation with water vapor by nonequilibrium plasma: Toward sustainable ammonia production. *ACS Sustain. Chem. Eng.* **2020**, *8*, 2996–3004. [CrossRef]
21. Toth, J.R.; Abuyazid, N.H.; Lacks, D.J.; Renner, J.N.; Sankaran, R.M. A plasma-water droplet reactor for process-intensified, continuous nitrogen fixation at atmospheric pressure. *ACS Sustain. Chem. Eng.* **2020**, *8*, 14845–14854. [CrossRef]
22. Haruyama, T.; Namise, T.; Shimoshimizu, N.; Uemura, S.; Takatsuji, Y.; Hino, M.; Yamasaki, R.; Kamachi, T.; Kohno, M. Non-catalyzed one-step synthesis of ammonia from atmospheric air and water. *Green Chem.* **2016**, *18*, 4536–4541. [CrossRef]
23. Winter, L.R.; Chen, J.G. N_2 fixation by plasma-activated processes. *Joule* **2021**, *5*, 300–315. [CrossRef]
24. Li, S.; Medrano, J.A.; Hessel, V.; Gallucci, F. Recent progress of plasma-assisted nitrogen fixation research: A review. *Processes* **2018**, *6*, 248. [CrossRef]
25. Bogaerts, A.; Tu, X.; Whitehead, J.C.; Centi, G.; Lefferts, L.; Guaitella, O.; Azzolina-Jury, F.; Kim, H.-H.; Murphy, A.B.; Schneider, W.F.; et al. The 2020 plasma catalysis roadmap. *J. Phys. D Appl. Phys.* **2020**, *53*, 443001. [CrossRef]
26. Rouwenhorst, K.H.R.; Engelmann, Y.; van't Veer, K.; Postma, R.S.; Bogaerts, A.; Lefferts, L. Plasma-driven catalysis: Green ammonia synthesis with intermittent electricity. *Green Chem.* **2020**, *22*, 6258–6287. [CrossRef]
27. Mehta, P.; Barboun, P.M.; Engelmann, Y.; Go, D.B.; Bogaerts, A.; Schneider, W.F.; Hicks, J.C. Plasma-catalytic ammonia synthesis beyond the equilibrium limit. *ACS Catal.* **2020**, *10*, 6726–6734. [CrossRef]
28. Van't Veer, K.; Engelmann, Y.; Reniers, F.; Bogaerts, A. Plasma-catalytic ammonia synthesis in a DBD plasma: Role of microdischarges and their afterglows. *J. Phys. Chem. C* **2020**, *124*, 22871–22883. [CrossRef]

29. Bai, M.; Zhang, Z.; Bai, X.; Bai, M.; Ning, W. Plasma synthesis of ammonia with a microgap dielectric barrier discharge at ambient pressure. *IEEE Trans. Plasma Sci.* **2003**, *31*, 1285–1291. [CrossRef]
30. Mizushima, T.; Matsumoto, K.; Sugoh, J.-I.; Ohkita, H.; Kakuta, N. Tubular membrane-like catalyst for reactor with dielectric-barrier-discharge plasma and its performance in ammonia synthesis. *Appl. Catal. A Gen.* **2004**, *265*, 53–59. [CrossRef]
31. Gómez-Ramírez, A.; Cotrino, J.; Lambert, R.M.; González-Elipe, A.R. Efficient synthesis of ammonia from N_2 and H_2 alone in a ferroelectric packed-bed DBD reactor. *Plasma Sources Sci. Technol.* **2015**, *24*, 065011. [CrossRef]
32. Aihara, K.; Akiyama, M.; Deguchi, T.; Tanaka, M.; Hagiwara, R.; Iwamoto, M. Remarkable catalysis of a wool-like copper electrode for NH_3 synthesis from N_2 and H_2 in non-thermal atmospheric plasma. *Chem. Commun.* **2016**, *52*, 13560–13563. [CrossRef]
33. Iwamoto, M.; Akiyama, M.; Aihara, K.; Deguchi, T. Ammonia synthesis on wool-like Au, Pt, Pd, Ag, or Cu electrode catalysts in nonthermal atmospheric-pressure plasma of N_2 and H_2. *ACS Catal.* **2017**, *7*, 6924–6929. [CrossRef]
34. Peng, P.; Li, Y.; Cheng, Y.; Deng, S.; Chen, P.; Ruan, R. Atmospheric pressure ammonia synthesis using non-thermal plasma assisted catalysis. *Plasma Chem. Plasma Process.* **2016**, *36*, 1201–1210. [CrossRef]
35. Kim, H.-H.; Teramoto, Y.; Ogata, A.; Takagi, H.; Nanba, T. Atmospheric-pressure nonthermal plasma synthesis of ammonia over ruthenium catalysts. *Plasma Process. Polym.* **2017**, *14*, 1600157. [CrossRef]
36. Akay, G.; Zhang, K. Process Intensification in ammonia synthesis using novel coassembled supported microporous catalysts promoted by nonthermal plasma. *Ind. Eng. Chem. Res.* **2017**, *56*, 457–468. [CrossRef]
37. Barboun, P.; Mehta, P.; Herrera, F.A.; Go, D.B.; Schneider, W.F.; Hicks, J.C. Distinguishing plasma contributions to catalyst performance in plasma-assisted ammonia synthesis. *ACS Sustain. Chem. Eng.* **2019**, *7*, 8621–8630. [CrossRef]
38. Wang, Y.; Craven, M.; Yu, X.; Ding, J.; Bryant, P.; Huang, J.; Tu, X. Plasma-enhanced catalytic synthesis of ammonia over a Ni/Al_2O_3 catalyst at near-room temperature: Insights into the importance of the catalyst surface on the reaction mechanism. *ACS Catal.* **2019**, *9*, 10780–10793. [CrossRef] [PubMed]
39. Li, S.; van Raak, T.; Gallucci, F. Investigating the operation parameters for ammonia synthesis in dielectric barrier discharge reactors. *J. Phy. D Appl. Phys.* **2019**, *53*, 014008. [CrossRef]
40. Michielsen, I.; Uytdenhouwen, Y.; Pype, J.; Michielsen, B.; Mertens, J.; Reniers, F.; Meynen, V.; Bogaerts, A. CO_2 dissociation in a packed bed DBD reactor: First steps towards a better understanding of plasma catalysis. *Chem. Eng. J.* **2017**, *326*, 477–488. [CrossRef]
41. Medford, A.J.; Vojvodic, A.; Hummelshøj, J.S.; Voss, J.; Abild-Pedersen, F.; Studt, F.; Bligaard, T.; Nilsson, A.; Nørskov, J.K. From the Sabatier principle to a predictive theory of transition-metal heterogeneous catalysis. *J. Catal.* **2015**, *328*, 36–42. [CrossRef]
42. Mehta, P.; Barboun, P.; Herrera, F.A.; Kim, J.; Rumbach, P.; Go, D.B.; Hicks, J.C.; Schneider, W.F. Overcoming ammonia synthesis scaling relations with plasma-enabled catalysis. *Nat. Catal.* **2018**, *1*, 269–275. [CrossRef]
43. Engelmann, Y.; van't Veer, K.; Gorbanev, Y.; Neyts, E.C.; Schneider, W.F.; Bogaerts, A. Plasma catalysis for ammonia synthesis: A microkinetic modelling study on the contributions of Eley-Rideal reactions. *ACS Sustain. Chem. Eng.* **2021**, *9*, 13151–13163. [CrossRef]
44. Wang, Z.; Zhang, Y.; Neyts, E.C.; Cao, X.; Zhang, X.; Jang, B.W.L.; Liu, C.-J. Catalyst preparation with plasmas: How does it work? *ACS Catal.* **2018**, *8*, 2093–2110. [CrossRef]
45. Gao, M.; Zhang, Y.; Wang, H.; Guo, B.; Zhang, Q.; Bogaerts, A. Mode transition of filaments in packed-bed dielectric barrier discharges. *Catalysts* **2018**, *8*, 248. [CrossRef]
46. Xie, Q.; Zhuge, S.; Song, X.; Lu, M.; Yu, F.; Ruan, R.; Nie, Y. Non-thermal atmospheric plasma synthesis of ammonia in a DBD reactor packed with various catalysts. *J. Phys. D Appl. Phys.* **2019**, *53*, 064002. [CrossRef]
47. Haley, S.M.; Tappin, A.D.; Bond, P.R.; Fitzsimons, M.F. A comparison of SEM-EDS with ICP-AES for the quantitative elemental determination of estuarine particles. *Environ. Chem. Lett.* **2006**, *4*, 235–238. [CrossRef]
48. Midgley, P.A.; Weyland, M. 3D electron microscopy in the physical sciences: The development of Z-contrast and EFTEM tomography. *Ultramicroscopy* **2003**, *96*, 413–431. [CrossRef]
49. Van Aarle, W.; Palenstijn, W.J.; De Beenhouwer, J.; Altantzis, T.; Bals, S.; Batenburg, K.J.; Sijbers, J. The ASTRA toolbox: A platform for advanced algorithm development in electron tomography. *Ultramicroscopy* **2015**, *157*, 35–47. [CrossRef]
50. Jiang, H.; Shao, T.; Zhang, C.; Li, W.; Yan, P.; Che, X.; Schamiloglu, E. Experimental study of Q-V Lissajous figures in nanosecond-pulse surface discharges. *IEEE Trans. Dielectr. Electr. Insul.* **2013**, *20*, 1101–1111. [CrossRef]
51. Peeters, F.J.J.; van de Sanden, M.C.M. The influence of partial surface discharging on the electrical characterization of DBDs. *Plasma Sources Sci. Technol.* **2014**, *24*, 015016. [CrossRef]
52. Herrera, F.A.; Brown, G.H.; Barboun, P.; Turan, N.; Mehta, P.; Schneider, W.F.; Hicks, J.C.; Go, D.B. The impact of transition metal catalysts on macroscopic dielectric barrier discharge (DBD) characteristics in an ammonia synthesis plasma catalysis reactor. *J. Phys. D Appl. Phys.* **2019**, *52*, 224002. [CrossRef]
53. Dai, W.; Reimann, J.; Hanaor, D.; Ferrero, C.; Gan, Y. Modes of wall induced granular crystallisation in vibrational packing. *Gran. Matter* **2019**, *21*, 26. [CrossRef]
54. Van Laer, K.; Bogaerts, A. Fluid modelling of a packed bed dielectric barrier discharge plasma reactor. *Plasma Sources Sci. Technol.* **2016**, *25*, 015002. [CrossRef]
55. Jardali, F.; Van Alphen, S.; Creel, J.; Ahmadi Eshtehardi, H.; Axelsson, M.; Ingels, R.; Snyders, R.; Bogaerts, A. NO_x production in a rotating gliding arc plasma: Potential avenue for sustainable nitrogen fixation. *Green Chem.* **2021**, *23*, 1748–1757. [CrossRef]

56. Zhu, X.; Hu, X.; Wu, X.; Cai, Y.; Zhang, H.; Tu, X. Ammonia synthesis over γ-Al_2O_3 pellets in a packed-bed dielectric barrier discharge reactor. *J. Phys. D Appl. Phys.* **2020**, *53*, 164002. [CrossRef]
57. Carrasco, E.; Jiménez-Redondo, M.; Tanarro, I.; Herrero, V.J. Neutral and ion chemistry in low pressure dc plasmas of H_2/N_2 mixtures: Routes for the efficient production of NH_3 and NH_4^+. *Phys. Chem. Chem. Phys.* **2011**, *13*, 19561–19572. [CrossRef]
58. Hong, J.; Aramesh, M.; Shimoni, O.; Seo, D.H.; Yick, S.; Greig, A.; Charles, C.; Prawer, S.; Murphy, A.B. Plasma catalytic synthesis of ammonia using functionalized-carbon coatings in an atmospheric-pressure non-equilibrium discharge. *Plasma Chem. Plasma Process.* **2016**, *36*, 917–940. [CrossRef]
59. Peng, P.; Cheng, Y.; Hatzenbeller, R.; Addy, M.; Zhou, N.; Schiappacasse, C.; Chen, D.; Zhang, Y.; Anderson, E.; Liu, Y.; et al. Ru-based multifunctional mesoporous catalyst for low-pressure and non-thermal plasma synthesis of ammonia. *Int. J. Hydrogen Energy* **2017**, *42*, 19056–19066. [CrossRef]
60. Shah, J.; Wu, T.; Lucero, J.; Carreon, M.A.; Carreon, M.L. Nonthermal plasma synthesis of ammonia over Ni-MOF-74. *ACS Sustain. Chem. Eng.* **2019**, *7*, 377–383. [CrossRef]
61. Patil, B.S.; van Kaathoven, A.S.R.; Peeters, F.J.J.; Cherkasov, N.; Lang, J.; Wang, Q.; Hessel, V. Deciphering the synergy between plasma and catalyst support for ammonia synthesis in a packed dielectric barrier discharge reactor. *J. Phys. D Appl. Phys.* **2020**, *53*, 144003. [CrossRef]
62. Hu, X.; Zhu, X.; Wu, X.; Cai, Y.; Tu, X. Plasma-enhanced NH_3 synthesis over activated carbon-based catalysts: Effect of active metal phase. *Plasma Process. Polym.* **2020**, *17*, 2000072. [CrossRef]
63. Shah, J.; Gorky, F.; Psarras, P.; Seong, B.; Gómez-Gualdrón, D.A.; Carreon, M.L. Enhancement of the yield of ammonia by hydrogen-sink effect during plasma catalysis. *ChemCatChem* **2020**, *12*, 1200–1211. [CrossRef]
64. Van Alphen, S.; Jardali, F.; Creel, J.; Trenchev, G.; Snyders, R.; Bogaerts, A. Sustainable gas conversion by gliding arc plasmas: A new modelling approach for reactor design improvement. *Sustain. Energy Fuels* **2021**, *5*, 1786–1800. [CrossRef]
65. Anastasopoulou, A.; Keijzer, R.; Patil, B.; Lang, J.; van Rooij, G.; Hessel, V. Environmental impact assessment of plasma-assisted and conventional ammonia synthesis routes. *J. Ind. Ecol.* **2020**, *24*, 1171–1185. [CrossRef]
66. Anastasopoulou, A.; Keijzer, R.; Butala, S.; Lang, J.; Van Rooij, G.; Hessel, V. Eco-efficiency analysis of plasma-assisted nitrogen fixation. *J. Phys. D Appl. Phys.* **2020**, *53*, 234001. [CrossRef]